Welding in the World (2024) 68:137–153
https://doi.org/10.1007/s40194-023-01637-w

RESEARCH PAPER

Study on microstructure characterization and mechanical properties of AISI 444 ferritic stainless steel joint by high-frequency pulse K-TIG welding

Zhihai Dong[1,2,3] · Ye Tian[1,4] · Tingting Hao[1,2] · YiWen Li[2,3] · JunYan Miu[2,3] · XinYing Cui[2,3] · Chenhe Chang[5,3] · Yunlong Chang[2,3]

Received: 11 October 2023 / Accepted: 16 November 2023 / Published online: 30 November 2023

Abstract
The research employed high-frequency pulse K-TIG for the welding of a 6mm thick AISI 444 ferritic stainless steel (FSS), and the welding process window was determined. Complete penetration was achieved in the state of single-pass autogenous welding. The influence law of technological parameters and weld appearance was analyzed. The microstructure characteristics of the weld zone (WZ) and heat-affected zone (HAZ) was investigated. Subsequently, the mechanical properties of welded joints are evaluated. It is found that the thermal conductivity of FSS is large, so the welding process window is relatively narrow, and the welding heat input determines whether the weld can achieve complete penetration. Both the WZ and HAZ contained secondary phase precipitates, including σ phase, χ phase, and Laves phases. The σ phase and χ phase were detected at the grain boundary, while the Laves phase was located both intragranularly and at the grain boundary.
In addition, NbC was detected in the HAZ. In addition, NbC was detected in the HAZ. The presence of a brittle-hard phase and coarse grain significantly affected the tensile properties and impact toughness at room temperature. The tensile strength of the weld is equivalent to 71% of the parent material, which is 561 MPa. Its average impact toughness value is 29 J, which is equivalent to 42% of the BM. Although the strength and toughness of FSS joints welded with high-frequency pulse K-TIG were somewhat inferior to the BM, the process displayed a marked improvement in welding efficiency.

Keywords High-frequency pulse K-TIG · Ferritic stainless steel · Microstructure characteristics · Mechanical property

1 Introduction

Ferritic stainless steel (FSS) contains almost no Ni and is a cheaper alternative to austenitic stainless steel (ASS). FSS has the advantages of high thermal conductivity, low linear expansion coefficient, and good stress corrosion resistance. At present, FSS has been widely used in pressure vessels, automotive industry [1–3], and other fields. However, the grain coarsening of the weld zone (WZ) in the welding process of FSS will seriously reduce the toughness, ductility, and corrosion resistance of the welded joint [4–6]. A possible solution to this predicament is employing filled austenitic welding wire techniques such as SMAW [7], GMAW [8, 9], and FCAW [10]. However, this method results in escalated welding materials wastage, reduced efficiency, and, hence, increased costs. TIG welding is an ideal welding method for FSS. This is because of the stable arc, high welding quality, and low welding heat input of TIG welding. However, due to the low arc energy of TIG

✉ Yunlong Chang
472212929@qq.com

1 Inner Mongolia Metal Material Research Institute, Baotou 014000, China

2 School of Materials Science and Engineering, Shenyang University of Technology, Shenyang 110870, China

3 Shenyang Collaborative Innovation Center project for Multiple Energy Fields Composite Processing of Special Materials, Shenyang 110027, China

4 Ningbo Surface Engineering Research Institute Co. LTD, Ningbo 315000, China

5 Liaoning Xinyuan Special Welding Technology Co. Ltd, Shenyang 110011, China

welding, it is not suitable for the welding of medium and thick plates, so only multi-pass gas tungsten arc welding can be used, which seriously affects the welding efficiency [11, 12]. Plasma arc welding (PAW) is a compression arc welding method. It has the advantages of fast cooling, fast welding speed, narrow weld area, and large penetration [13, 14]. Compared with TIG welding, PAW has a more concentrated arc energy density and higher arc stiffness. Therefore, the heat provided per unit length is smaller, and a relatively finer weld structure can be obtained, which is more suitable for FSS welding [15]. Zhu et al. [16] adopted a perforated-plasma-arc-welded welding process to achieve complete penetration of 8 mm thick 00Cr11NbTi FSS stainless steel. The experimental results show that the smooth surface of the weld can be obtained under the premise of good assembly. KÖSE et al. [17] analyzed the impact of varied heat inputs on the PAW welding of FSS, ascertaining reduced tensile strength and hardness of the welded joints with elevated heat input. Post-weld heat treatment, a further reduction in tensile strength was observed, owing to the welding microstructure's softening and transformation after enduring 770 °C for 60 min. Nevertheless, PAW's excessive arc stiffness and fast welding speed predispose the weld to biting defects and increased porosity, respectively. In addition, the welding process subjects the weld to substantial stretching or twisting force, predisposing it to cracking [18]. Hariharan et al. [19] studied the influence of the PAW process on the corrosion resistance and strength of AISI 409 FSS joints. The response surface method is used to obtain the best combination of welding parameters, which maximizes the strength of welded joints and minimizes the corrosion rate. Therefore, it is imperative to establish a balanced confluence of PAW welding parameters, including ion gas flow, welding current, welding speed, and protecting gas flow. Such precision, however, results in a complex process, limiting its applications.

Deep penetration welding techniques such as electron beam welding (EBW) [20, 21] and laser beam welding (LBW) [5, 22] enhance the efficiency of medium and thick plate welding. However, these welding methods are not suitable for field operation, the equipment is complex, the production cost is high, and the practical application is limited [23].

K-TIG is a kind of keyhole deep penetration welding method derived from traditional TIG welding. Different from traditional TIG, in order to carry greater welding current (>300A), the K-TIG welding gun uses a larger diameter tungsten electrode. The welding gun can be applied to strengthen the tungsten electrode cooling system. High current causes arc self-compression, which, combined with an efficient cooling system, results in an arc compression effect [23]. The arc energy and arc pressure are increased after compression. The larger arc pressure causes the liquid metal in the molten pool to flow around and pit until it penetrates. Under the combined action of arc pressure, the gravity of the liquid metal, and the surface tension of the liquid metal, the small hole remains in dynamic equilibrium [24, 25]. During the welding process, the keyhole is kept open, and part of the welding arc spills over the back of the workpiece, as shown in Fig. 1a. It has been proved that K-TIG can achieve full penetration of medium and thick plates in the state of autogenous welding [23]. Compared with LBW, EBW, and PAW, K-TIG welding has easy operation, low cost, and low pre-welding assembly requirements, which is suitable for field work [24, 26].

It has been proved that K-TIG has been successfully used for single-pass welding of medium and thick plates of Zr

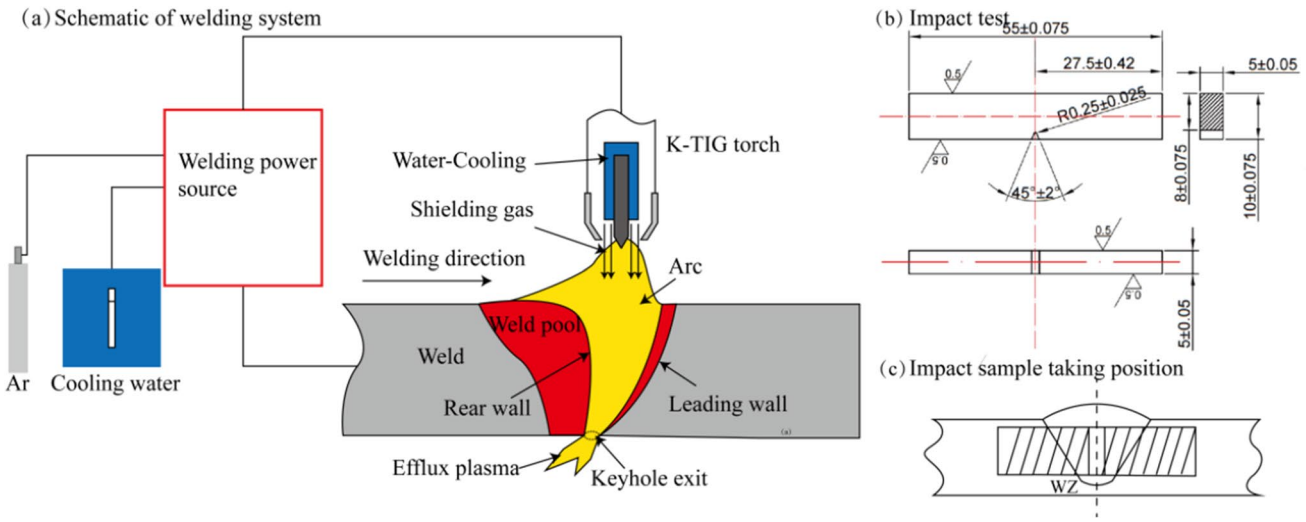

Fig. 1 **a** K-TIG experimental system. **b** Impact test specimen. **c** Impact sample sampling location

[27], Ti [28], and other materials. Fei et al. [29] used K-TIG to achieve complete penetration of armour grade quenched and tempered steel in the state of autogenous welding. The weld is composed of dendrite and bainite structure, the hardness of the weld is increased, and the ballistic performance is improved. In recent years, scholars have conducted a lot of research on the K-TIG welding process of stainless steel. Feng et al. [26] used K-TIG to weld 316L ASS with a thickness of 6–13 mm, employing an I-groove without filler wire, and accomplished single-pass welding. The post-welding tensile strength and impact toughness were similar to the base metal (BM), demonstrating K-TIG as a high-quality, efficient method for welding AISI 316L ASS. Cui et al. [30] achieved one-side welding with back formation on 8 mm thick 2205 duplex stainless steel (DSS) using K-TIG at welding speeds of 280–340 mm/min, resulting in welds with good plasticity. Zmitrowicz et al. [31] confirmed K-TIG's applicability for one-side welding with back formation on 1.4462 duplex steel, showing increased ferrite content in the K-TIG weld zone, but similar heat-affected zone (HAZ) microstructures to traditional TIG welding. The properties of the welded joint met the requirements. Later, Cui et al. [32] studied K-TIG welding of 4 mm thick 304 ASS, achieving the "one pulse, one open keyhole" K-TIG welding process under square wave pulse welding current, and obtained a qualified joint at a low average current. Current research on K-TIG stainless steel welding primarily concerns ASS and DSS. However, studies on FSS, which has higher thermal conductivity, are limited, making the exploration of high-frequency pulse K-TIG welding of FSS of significant research value.

In this investigation, we employed high-frequency pulse K-TIG welding to enhance the potential for superior weld efficiency in AISI 444 FSS. We thoroughly examined the K-TIG welding process window for AISI 444 FSS. The study also scrutinized the microstructure characterization and mechanical properties of the welded joints created under varying parameters. This research offers novel welding methodologies and insights to address the challenge of highly efficient and superior quality welding of medium and heavy plate FSS.

2 Materials and experiment methods

The BM for this experiment is AISI 444 FSS, the chemical composition of which is illustrated in Table 1. The sample plate measures 150 mm × 80 mm × 6 mm. Figure 1a depicts the high-frequency pulse K-TIG welding system used. The welding power supply, a self-developed high-frequency pulse K-TIG system, offers an adjustable welding current range of 10 to 1000 A.

Before the welding process commenced, the test plate was meticulously polished within a 30 mm radius on either side of the weld line using sandpaper and subsequently cleaned with acetone. The experiment employed plane position welding, with the test plate secured using a welding fixture to mitigate thermal deformation. Samples from the welded joints were obtained through wire cutting. These metallographic samples were polished using sandpaper with a mesh range of 400# to 2000# and further refined with a 2.5 μm diamond suspension. Aqua regia was utilized as the corrosion solution, with an exposure time of 40 s. The Olympus Optical microscope (OM), Hitachi S-3400N scanning electron microscope (SEM), and X-ray diffraction (XRD) were used for examining the appearance, microstructure, tensile fracture morphology, and impact fracture morphology of the weld. The tensile sample was prepared following the GB/T 2651-2008 standard, and the tensile test was conducted on the WDW-100 universal testing machine at a tensile speed of 1 mm/min. Charpy impact toughness specimens were prepared in accordance with GB/T 2650-20081 (as depicted in Fig. 1b, c). Two Charpy V impact toughness samples measuring 55 mm × 10 mm × 2.5 mm were extracted from the WZ, and the impact test was performed at room temperature.

3 Results and discussion

3.1 Study on high-frequency pulse K-TIG welding process window

In the formation of a keyhole during K-TIG welding, a dynamic balance must be maintained among the arc pressure, surface tension, and gravity of the liquid metal in the molten pool. For the keyhole to advance steadily, it is essential to maintain the matching of welding parameters such as the diameter and spacing of the tungsten electrode, the angle of the tungsten tip, welding current, welding speed, and argon flow rate. This necessitates a narrow welding process window, which requires thorough exploration. Following extensive exploration experiments and literature reviews, a welding speed between 4.5 and 6.5 mm/s was chosen, assuming other welding parameters remain constant. This experiment employed a cerium tungsten electrode with a diameter of 6 mm and a tungsten tip angle of 90°. Given

Table 1 Chemical composition of AISI444 FSS (wt%)

Cr	Mo	Nb	Si	Mn	C	N	S	P
18.0	**1.8**	**0.30**	**0.32**	**0.25**	**0.008**	**0.007**	**0.001**	**0.020**

Table 2 Process parameters of high-frequency pulse K-TIG welding AISI 444 FSS

No.	Welding current (A)	Welding speed (mm/s)	Arc length (mm)
1	610	4.5	0.5
2	620	4.5	0.5
3	620	5.5	0.5
4	630	5.5	0.5
5	640	5.5	0.5
6	650	5.5	0.5
7	660	5.5	0.5
8	620	6.5	0.5
9	660	6.5	0.5
10	690	6.5	0.5

that FSS exhibits high thermal conductivity and the welding arc is prone to dispersion, reducing the distance between the tungsten pole and the workpiece helps mitigate energy loss. The keyhole's constraining influence on the arc, as established through repeated experiments, led to the selection of a 0.5 mm tungsten pole spacing. In this experiment, argon gas with a purity of 99.999% was used for shielding, with a flow rate set to 25 L/min. Excessive or insufficient gas flow rates can lead to air inclusion, thereby affecting the welding quality. The specific process parameters for each group in the high-frequency pulse K-TIG welding test are detailed in Table 2.

Figure 2 displays the weld appearance of AISI 444 FSS welded using high-frequency pulse K-TIG at various parameters. All samples were successfully welded in a single pass, with the majority exhibiting good quality. The predominant weld colors were black and silver-white, attributed to the excessively high welding current and inadequate gas shielding. The substantial welding current often resulted in an arc

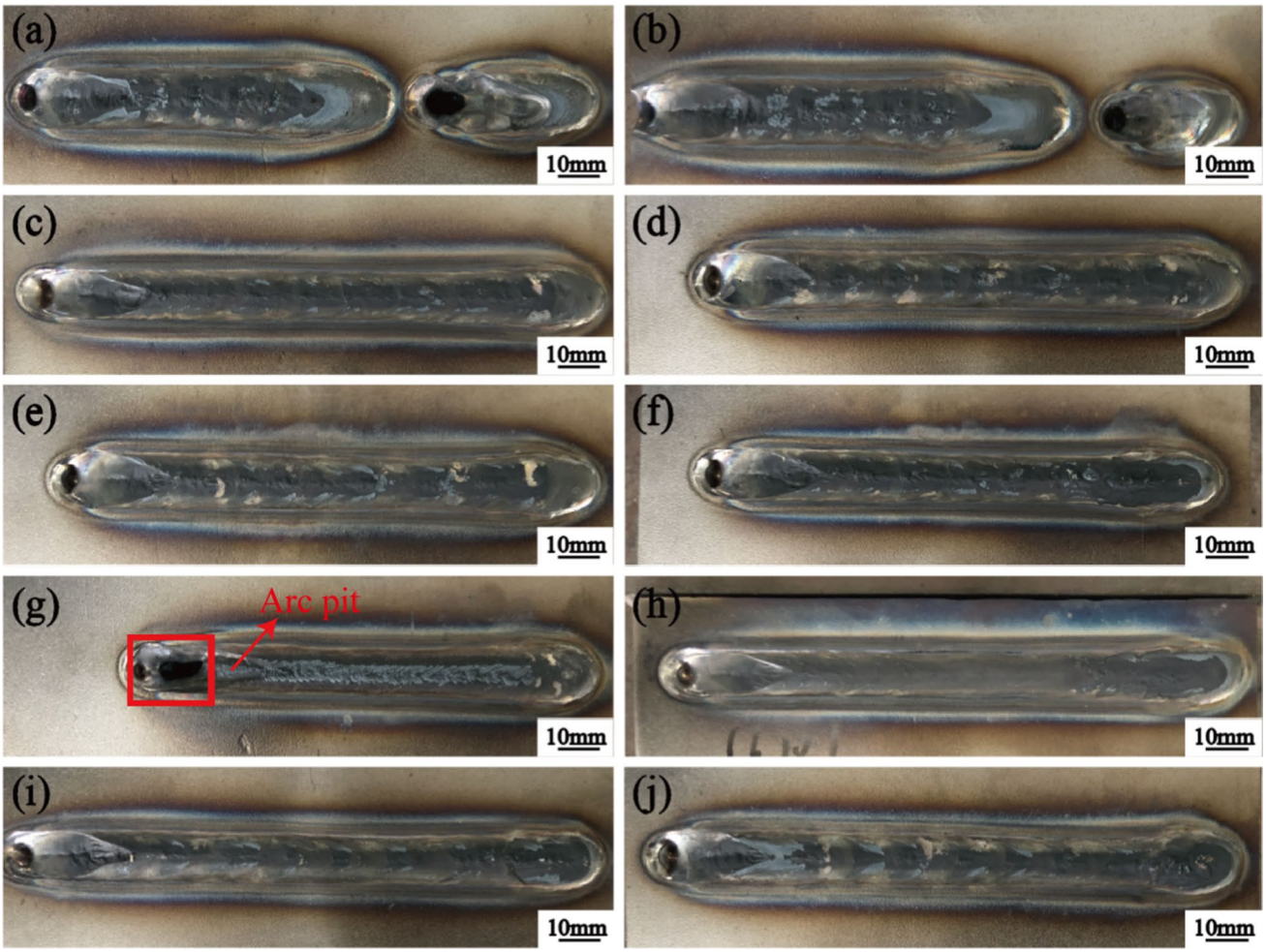

Fig. 2 AISI 444 FSS under different welding parameters high-frequency pulse K-TIG weld appearance. **a** No. 1, **b** No. 2, **c** No. 3, **d** No. 4, **e** No. 5, **f** No. 6, **g** No. 7, **h** No. 8, **i** No. 9, **j** No. 10

quenching pit at the weld's end. Specifically, in Fig. 2g, the weld's tail exhibits burn-through, its middle is convex, and overall, the quality is substandard, stemming from excessive heat input during welding. Notably, a reduced welding speed correlates with increased heat input.

Based on a range of tests conducted under varying welding parameters, the process window for the AISI 444 FSS high-frequency pulse K-TIG welding is depicted in Fig. 3. The blue region in the figure indicates a combination of parameters that yield a qualified weld. A qualified weld is defined as one that is fully penetrated without any signs of weld collapse. However, outside this designated blue region, there is a higher risk of weld collapse or incomplete welding. As highlighted in literature [23], the welding process window is primarily determined by the heat input of the welding process. An excessively high welding current or an excessively slow welding speed can increase the welding heat input, thereby disrupting the dynamic balance of the small hole and leading to weld collapse. Conversely, a welding current that is too low or a welding speed that is too fast can result in a reduced welding heat input, preventing the formation of small holes and thereby causing incomplete welding. These observations are substantiated by the cross-sectional morphology of the AISI 444 FSS high-frequency pulse K-TIG weld under various welding parameters.

Figure 4 illustrates the appearance of high-frequency pulse K-TIG welds on AISI 444 FSS under various welding parameters. Unlike the conventional TIG weld appearance, the K-TIG weld exhibits a "funnel shape," wider at the top and narrower towards the bottom, enabling complete penetration and formation on both sides through a single-side welding process. However, when compared to LAW and EBW, the K-TIG weld profile is broader, attributed to

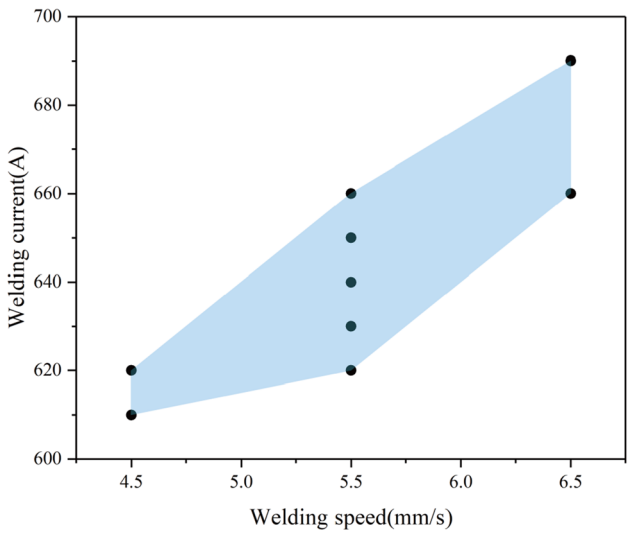

Fig. 3 AISI 444 FSS high-frequency pulse K-TIG welding process window

the relatively dispersed energy density of the K-TIG arc. According to the welding heat input formula (1), the welding heat input of 10 groups of tests can be calculated, and the measured welding heat input is successively No. 2>No. 1>No. 7>No. 10>No. 6>No. 9>No. 5>No. 4>No. 3>No. 8. No. 2, No. 7, No. 6, and No. 10 specimens are completely melted through; No. 9, No. 5, No. 4, No. 3, and No. 8 are not melted through, which is consistent with the conclusion above.

$$Q = \frac{U \bullet I}{v}\eta \tag{1}$$

Where Q is the welding heat input, J/cm; U is the arc voltage, V; I is the welding current, A; v is the welding speed, cm/s; η is the power coefficient of arc.

Figure 4 illustrates the impact of welding parameters on weld appearance. Samples No. 2, No. 3, and No. 8 (as seen in Fig. 4b, c, and h) display the weld appearance at a constant welding current of 620A, with welding speeds escalating from 4.5 to 6.5mm/s. An increase in speed leads to reduced weld penetration and a lower depth-to-width ratio. This occurs because a slower welding speed, correlating with higher welding heat input, enhances the energy transferred by the arc, facilitating more extensive melting. Consequently, a wider weld is formed, characterized by complete melting and an increase in excess weld metal at the weld back due to the flow of substantial metal beneath the hole. Conversely, at higher speeds, the arc's penetration capability diminishes, making it challenging to form a smaller pool and complete penetration. Samples No. 3 to No. 7 (shown in Fig. 4c~g) represent high-frequency pulse K-TIG weld appearance at a fixed speed of 5.5 mm/s and varying welding currents from 620 to 660 A. Figure 5 demonstrates that as the welding current increases, both weld penetration and the depth-to-width ratio enlarge, attributable to enhanced arc penetration. This phenomenon, observed in ASS welding, aligns with findings by Feng [26] and Unnikrishnan [33].

When the welding current is between 620 and 640 A, the lower current results in inadequate arc penetration, preventing the plasma from being ejected from the weld's back and inhibiting the formation of a small hole, ultimately resulting in a lack of weld penetration. However, when the welding current is increased to 650 A, the increased welding arc pressure forms a small hole in the weld pool, enabling single-sided welding with back formation. Further increasing the welding current to 660 A causes the weld surface to become concave due to excessive current. Fei et al. [29] posited that surplus heat input and arc force could disrupt the force balance within the small hole channel, leading to the collapse of the weld in specific areas.

In conclusion, the heat input during welding determines whether the high-frequency pulse K-TIG weld can achieve complete penetration. The welding current primarily

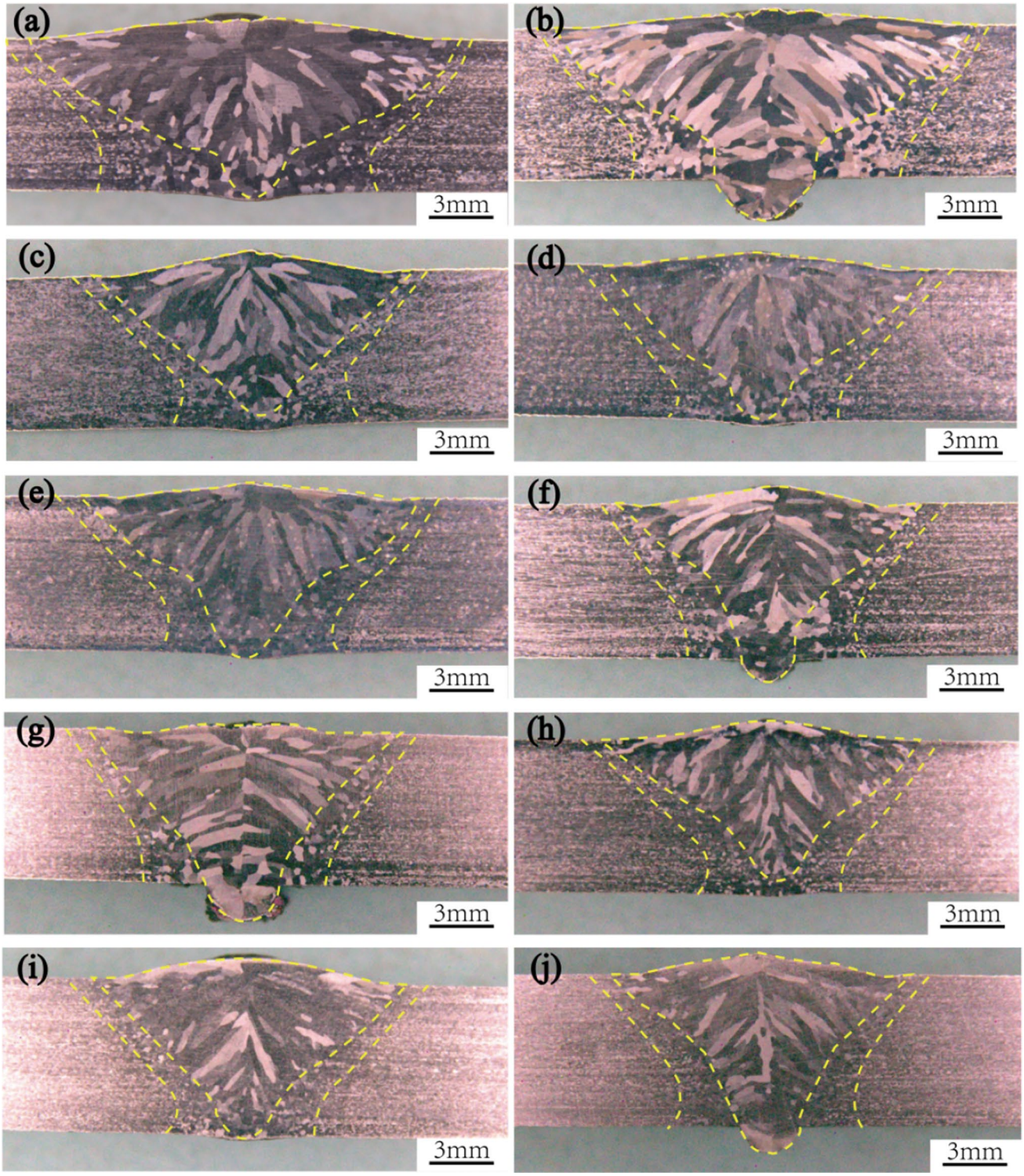

Fig. 4 AISI 444 FSS high-frequency pulse K-TIG weld appearance under different welding parameters

influences the size of the weld penetration, while the welding speed mainly impacts the weld width. Therefore,

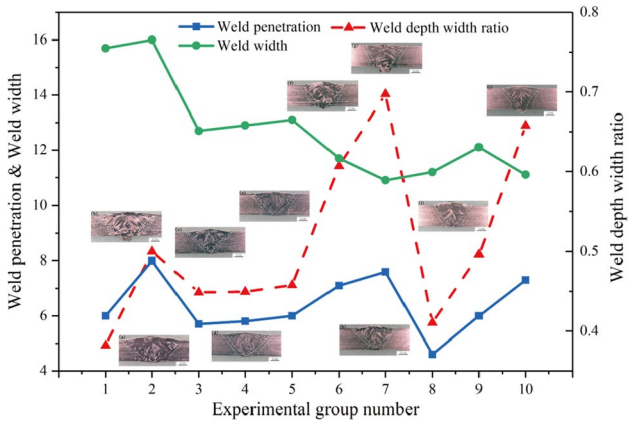

Fig. 5 Geometric dimensions of AISI 444 FSS high-frequency pulse K-TIG weld under different welding parameters

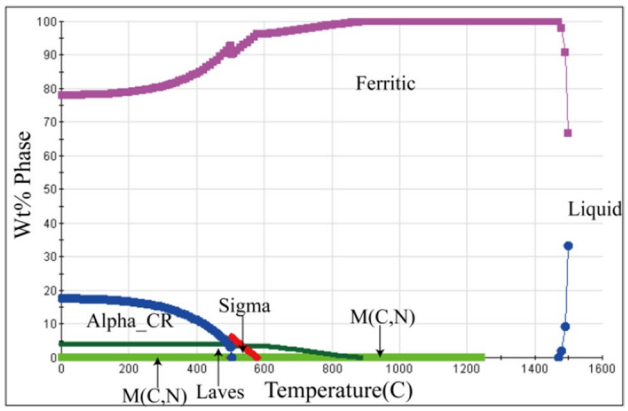

Fig. 6 Equilibrium phase diagram of AISI444 FSS

within the optimal welding process window, the appropriate welding parameters should be selected to achieve the desired weld forming quality.

3.2 Microstructure

3.2.1 Microstructure prediction

The Schaeffler diagram delineates the quantitative correlation between the chemical composition (excluding nitrogen) of stainless steel weld metal and its resultant phase structure. It utilizes the concentrations of austenitic elements (such as Ni, C, Mn) and ferritic elements (such as Cr, Mo, Si) to compute the chromium equivalent (Cr_{eq}) and nickel equivalent (Ni_{eq}). These calculations facilitate the determination of the phase composition and proportion within the weld microstructure by referencing the Schaeffler microstructure chart. Equations (2) and (3) provide the computational methods for Cr_{eq} and Ni_{eq}, respectively. Upon integrating the chemical compositional data from Table 1 into these equations, the results yield A=20.43 and B=0.365. Analysis of the Schaeffler diagram indicates that the weld microstructure of AISI444 FSS is exclusively ferritic [20].

$$Cr_{eq} = Cr\% + Mp\% + 1.5 \times Si\% + 0.5Nb\% \quad (2)$$

$$Ni_{eq} = Ni\% + 30 \times C\% + 0.5 \times Mn\% \quad (3)$$

The Schaeffler microstructure diagram primarily accounts for the influence of chemical composition on microstructure. However, it lacks precision in predicting the weld microstructure of AISI444 FSS under varying conditions such as changes in alloying element morphology, welding methods, and joint configurations. For instance, the precipitation of alloying elements as compounds does not alter the phase ratio. To enhance the accuracy of weld microstructure predictions for AISI444 FSS, the JMatPro 7.0 material property simulation software was employed to model the equilibrium phase diagram at 1500 ℃. Figure 6 illustrates that above 800 ℃ during the liquid phase cooling of AISI444 FSS, the weld microstructure predominantly exhibits a single ferritic phase with minimal carbon or nitride precipitation. Upon cooling to a range of 800 to 500 ℃, the σ phase, an Fe-Cr intermetallic compound, may manifest within the weld tissue. This phase enhances weld strength, yet it concurrently leads to a significant reduction in plastic toughness. When the cooling temperature falls below 500 ℃, a combination of α' and Laves phases might materialize within the weld tissue. The α' phase is a Cr-enriched intermetallic compound. Silva et al. [7] employed the time-temperature precipitation (TTP) diagram of FSS, as depicted in Fig. 7, to forecast the precipitation of the second phase in FSS welds. Their research revealed that Nb, typically present in welds as a carbide or nitride, will recombine with carbon and nitrogen upon reaching a temperature exceeding 1100 ℃ (welding

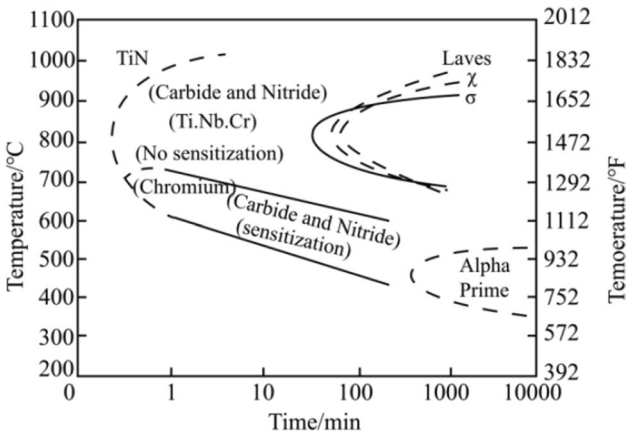

Fig. 7 Isothermal precipitation diagram of secondary phases in FSS [7]

zone temperature greater than 1100 ℃). This reaction leads to the formation of the Laves phase with iron, chromium, and other elements.

Zhang et al. [9] identified that FSS exhibits sensitivity to intergranular corrosion. To mitigate this issue, elements such as Nb or Ti, renowned for their stability, are typically introduced to foster the generation of their respective carbides, thereby suppressing Cr carbide formation and averting intergranular Cr depletion. Given the low concentration of C and N in the material tested in this study, only niobium was introduced, and a single stabilization approach was employed. Consequently, Nb carbides and nitrides might precipitate in the BM or proximal to the HAZ. Post-welding, the weld naturally cools to room temperature at a swift rate. When considered in conjunction with the Schaeffler structure diagram, the equilibrium phase diagram simulated by JMatPro 7.0 software, and the TTP diagram, it can be inferred that the structure of the AISI444 FSS joint primarily consists of a ferrite structure, with concurrent precipitation of the σ phase, x phase, Laves phase, and a' phase.

3.2.2 Microstructure of K-TIG joint

In the welding process, parameters yielding the best weld formation quality were selected and the weld's microstructure was analyzed. Figure 8 displays the microstructure of the fully penetrative high-frequency pulse K-TIG weld in Sample No. 6. As depicted in Fig. 8a, the WZ primarily

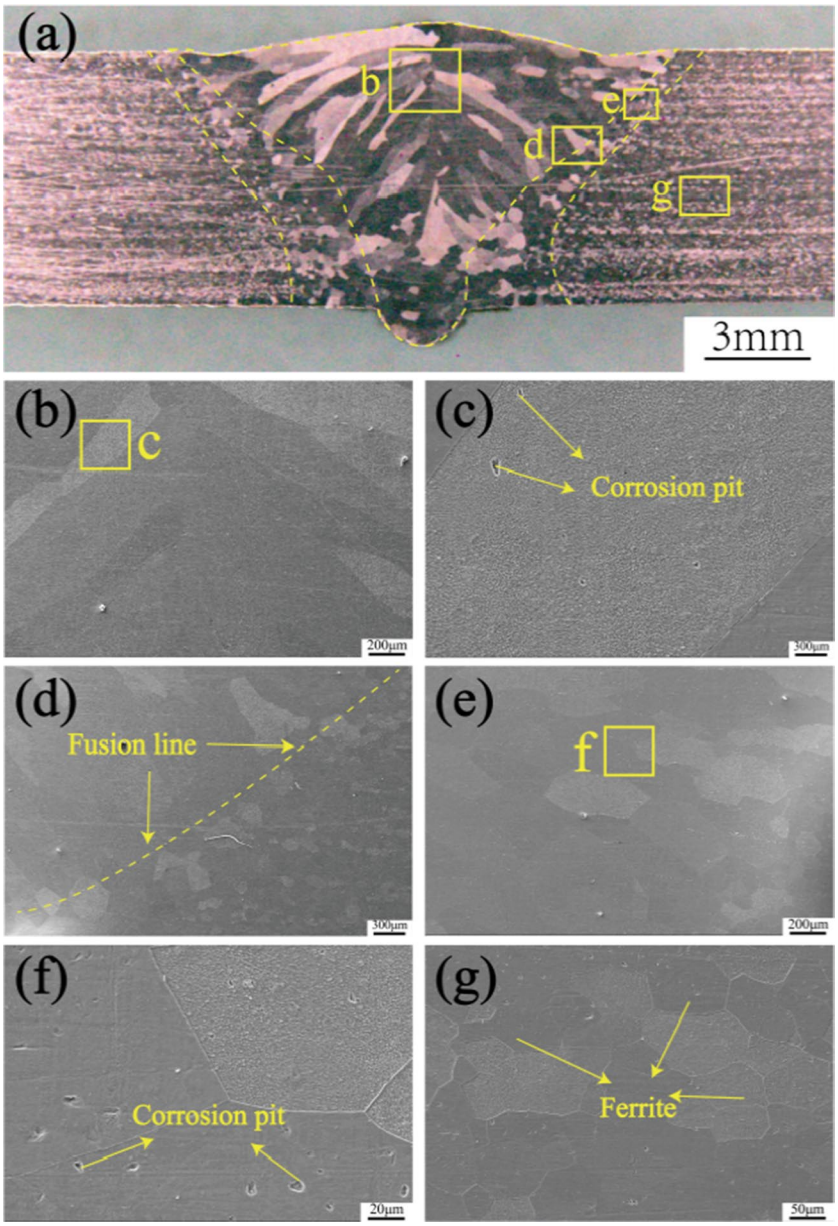

Fig. 8 Microstructure of high-frequency pulse K-TIG weld: **a** weld cross-section; **b** WZ; **c** precipitate phase is precipitated in the WZ; **d** FZ; **e** HAZ; **f** precipitate phase is precipitated in the HAZ; **g** BM (No. 5)

consists of large columnar ferrite grains and a minority of equiaxed crystals. The substantial heat input from high-frequency pulse K-TIG welding results in a large molten pool volume, subsequently leading to slow cooling and crystallization rates post-welding. This condition, in line with the theory of component supercooling, favors columnar crystal formation over equiaxed crystals [34]. Further analysis from Fig. 8b and c reveals that the weld's grain growth aligns with the direction of the fastest cooling rate in the weld pool, without any solid phase transformation occurring during solidification. Additionally, precipitated phases were observed in the WZ under high magnification. Figure 8d highlights the fusion line, demarcated by a dashed white line, which separates the WZ from the HAZ, with a notable difference in grain sizes between these areas. Figure 8e illustrates the HAZ, characterized by equiaxed crystals. Due to the high heat input of high-frequency pulse K-TIG welding, the grains in the HAZ appear coarser. Figure 8a demonstrates that the HAZ at the upper part of the weld is notably narrow, with minimal change in grain size. This can be attributed primarily to the high thermal conductivity of FSS and secondarily to the concentrated energy density of the K-TIG arc, which reduces the duration of high-temperature exposure in the HAZ. Conversely, the HAZ at the lower part of the weld exhibits a larger grain size. This is due to the keyhole formation facilitating the transfer of arc energy to the keyhole's bottom, as referenced in [35], resulting in higher heat input at this location. Furthermore, the rapid cooling rate of the HAZ contributes to its limited extent. Corrosion pits after corrosion were found in the HAZ, as shown in Fig.8f.

The preceding analysis indicates that weld tissue may incorporate secondary phases, prompting further magnification for detailed observation. Examination revealed precipitated phases at both grain boundaries and within the crystalline structure of the WZ and the HAZ. Figure 9a illustrates the WZ microstructure in FSS, where precipitates are noted along the grain boundaries. EDS facilitated the quantitative analysis, identifying the grain boundary precipitates as the σ phase. This identification is founded on the propensity of the σ phase to precipitate at ferritic grain boundaries as a metal Fe-Cr phase characterized by chromium enrichment. Furthermore, the σ phase's growth within the grain reaches a saturation point, prompting intragrain precipitation. Sourmail et al. [7, 36] have demonstrated that σ phase formation is favored by a Cr mass fraction of 25 to 30% and a precipitation temperature range of 600 to 1050 °C. The presence of Cr, Nb, Mo, and similar elements in FSS, coupled with the elemental enrichment and temperature conditions in welding, creates an ideal environment for σ phase development.

Figure 9a and b illustrate the formation of a minute precipitate at the grain boundaries, identified as the x phase. Lu et al. [37] observed that this phase typically manifests as nanoscale rods along grain boundaries. Ge et al. [38, 39] posited that the presence of Mo in FSS facilitates the x phase precipitation, particularly within a Mo mass fraction ranging from 15 to 25% and a precipitation temperature of 600to 900 ℃. Studies indicate that the x phase precipitates more rapidly and precedes the σ phase [38, 40]. Furthermore, the x phase is deemed a precursor that promotes the formation of the σ phase [7], as it exists in a metastable state and decomposes

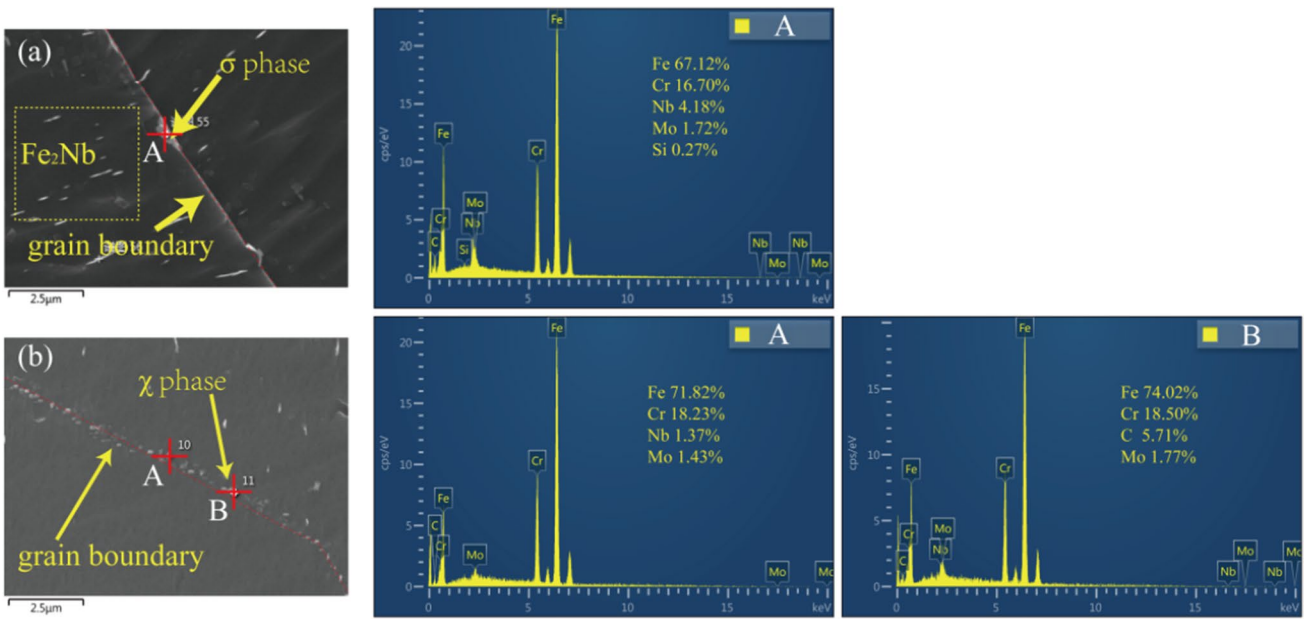

Fig.9 Microstructure and EDS analysis of precipitated phase in the WZ of high-frequency pulse K-TIG joint: **a** σ phase; **b** x phase

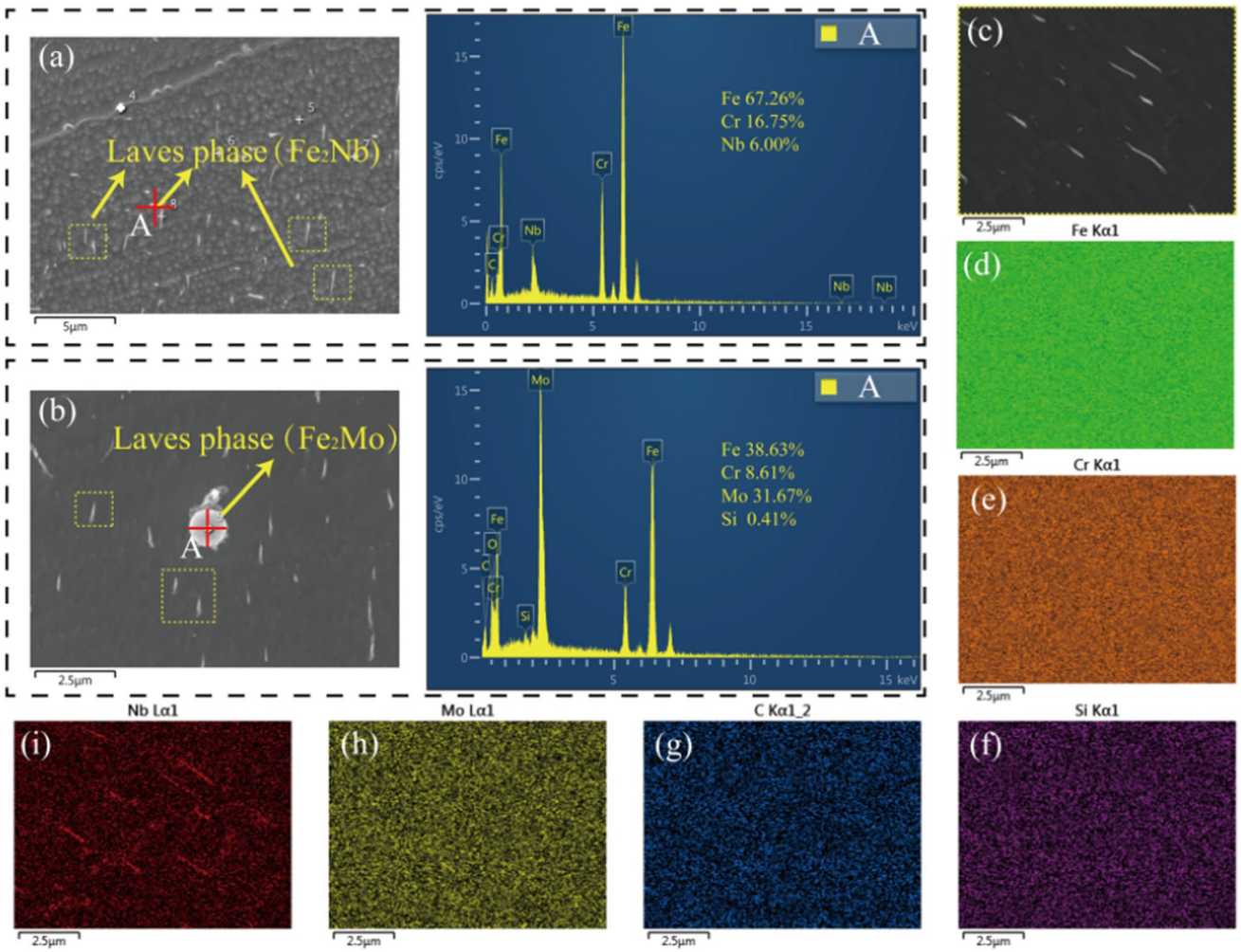

Fig.10 EDS analysis of precipitated phase in the WZ of high-frequency pulse K-TIG joint: **a**, **b** EDS analysis of precipitated phase in WZ; **c~i** elemental maps of selected area

over time and temperature, releasing substantial amounts of Mo and Cr elements necessary for the σ phase development.

A substantial amount of acicular precipitates was observed in the WZ of the high-frequency pulse K-TIG connection, as evidenced in Fig. 10. EDS analysis (Fig. 10a) revealed that these precipitates predominantly consist of Cr, Fe, Nb, and other elements, predominantly located within the crystal lattice and, to a lesser extent, along grain boundaries. This distribution suggests that the precipitates are of the Laves phase. Ma et al. [41] emphasized that the Laves phase, in comparison to the σ phase and x phase, is characterized by a notably higher concentration of Nb. Furthermore, in the Laves phase, the mass fractions of Nb and Mo are higher than those in the surrounding matrix, typically precipitating at dislocations and substructures. EDS mapping (Fig. 10c~i) of the WZ indicates elemental segregation in these precipitates, with a pronounced segregation of Nb, corroborating that the Laves phase in the crystals could be Fe_2Nb. Additionally, as depicted in Fig. 10b, spherical precipitates, rich in Mo, were also identified within the grains in the WZ.

In their study, Juuti et al. [42] posited that the Laves phases in FSS are likely composed of Fe_2Nb and Fe_2Mo, with Si enrichment in the precipitates. This suggests that these sediments are also predominantly Fe_2Mo Laves phases. Both σ and x phases, along with Laves phases, contribute to reduced toughness and increased hardness in FSS. Figure 11a reveals that, besides the needle-like Laves phase, the WZ contains substantial precipitates, likely the Cr-rich phase a, as inferred from earlier analysis (see Fig. 6). It is noted that when the Cr concentration in FSS exceeds 12%, 475 ℃ embrittlement occurs during prolonged exposure at temperatures between 340 and 516 ℃. This embrittlement is attributed to the decomposition of ferrite into Cr-rich a' and Fe-rich a phases, both sharing the same bcc structure. The Cr content in the a' phase

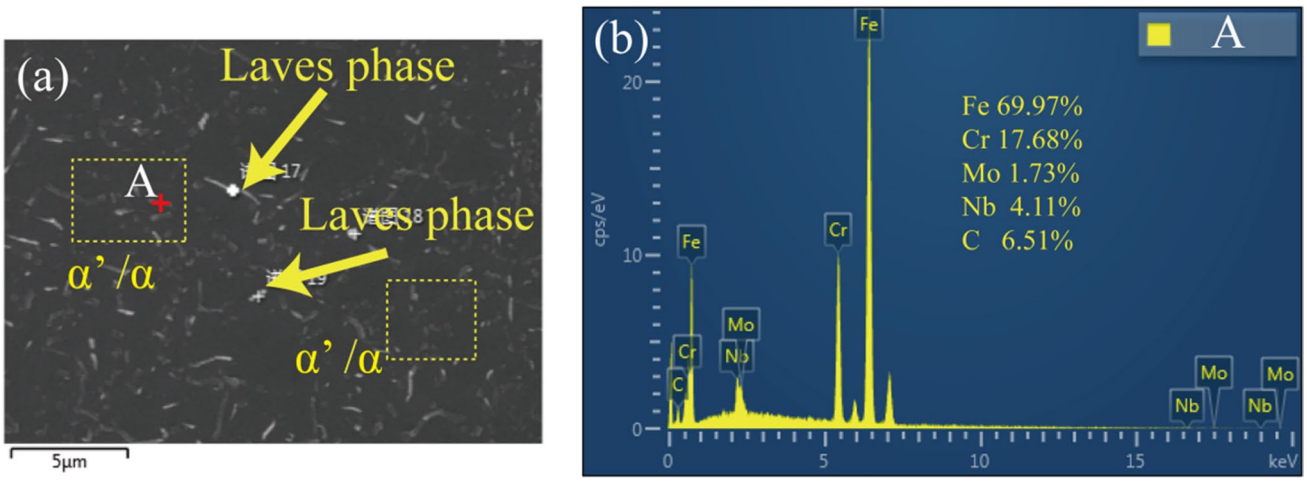

Fig.11 EDS analysis of precipitated phase in the WZ of high-frequency pulse K-TIG joint: **a** Mixed phase of Laves phase and *a′/a* phase in WZ; **b** EDS of *a* phase

varies between 61 and 83%. However, the higher Fe content observed in the EDS in Fig. 11b indicates the presence of an Fe-rich *a* phase at this location.

The σ phase, *x* phase, and Laves phase are also identified in the HAZ of K-TIG welds under high-frequency pulse conditions. Contrary to the WZ, an additional precipitating phase is discernible, as illustrated in Fig. 11. It is apparent that ellipsoidal, rod-like precipitates are uniformly distributed within the grain boundaries and crystals. Generally, the HAZ temperature during welding exceeds 900 ℃. Based on the information in Fig. 7, carbides or nitrides are likely to form under these thermal conditions. Previous research by Yan et al. [43] discovered the presence of NbC within the grain boundaries and crystals of ferrite in FSS containing Nb. Meanwhile, Saha et al. [44] showed that undissolved carbon elements, during the high-temperature cooling of FSS, form (Ti, Nb) C with Nb and Ti. This (Ti, Nb)C contributes to dispersion strengthening and impedes sensitization in FSS. The EDS analysis, presented in Fig. 11a, reveals a high peak of Nb, and segregation of Nb, C, and Mo elements at the sediment's location, identified through surface scanning (Fig. 11c~i). The sediment is finally determined to be NbC. Additionally, NbC might also originate from the BM, as depicted in Fig. 11b. Within FSS, Nb enhances the strength and impacts the tough-brittle transition temperature. Particularly, Nb has a propensity to combine preferentially with C, forming NbC, which consequently reduces the intergranular corrosion tendency of FSS. Despite the HAZ potentially attaining a maximum temperature of 1100 ℃, NbC, with its high melting point, is resistant to dissolution. Moreover, NbC plays a dual role in both pinning grain boundaries and impeding grain boundary movement, providing another explanation for the restricted growth of HAZ grains.

To substantiate the microstructure of the AISI444 FSS welded joint, we conducted a phase analysis of the WZ and HAZ using XRD, as depicted in Fig. 12. Despite the fact that smoothed peaks are more readily discernible, we preserved the integrity of the original data by abstaining from any modifications. This was achieved by cross-referencing the XRD diffraction pattern with the PDF card. The peak values and positions of each phase are listed in Table 3. Upon examination, the phase composition of the WZ and HAZ appears to be quite similar, primarily featuring $a-Fe$ as the matrix, which exhibits a high peak value. The Jade9 software identified several peaks within these more pronounced peaks. Secondary phases such as σ phase, *x* phase, and Laves phase precipitated within the matrix are also evident, but they exhibit lower peak values due to the minor content and size of these secondary phases. Furthermore, HAZ contains a trace amount of NbC. The XRD phase analysis results of these precipitated phases align well with our previous analyses (Fig. 13).

3.3 Mechanical properties of joint

3.3.1 Tensile strength

Figure 14 delineates the tensile curves corresponding to the welded joints of BM and Joint No.6. It is a common practice to categorize the tensile curves of steel into three types: continuous transition, uniform yield, and non-uniform yield. Upon examination of the stretching curve, it is apparent that the tensile curve progresses through four distinct stages: elastic deformation, plastic deformation, non-uniform plastic

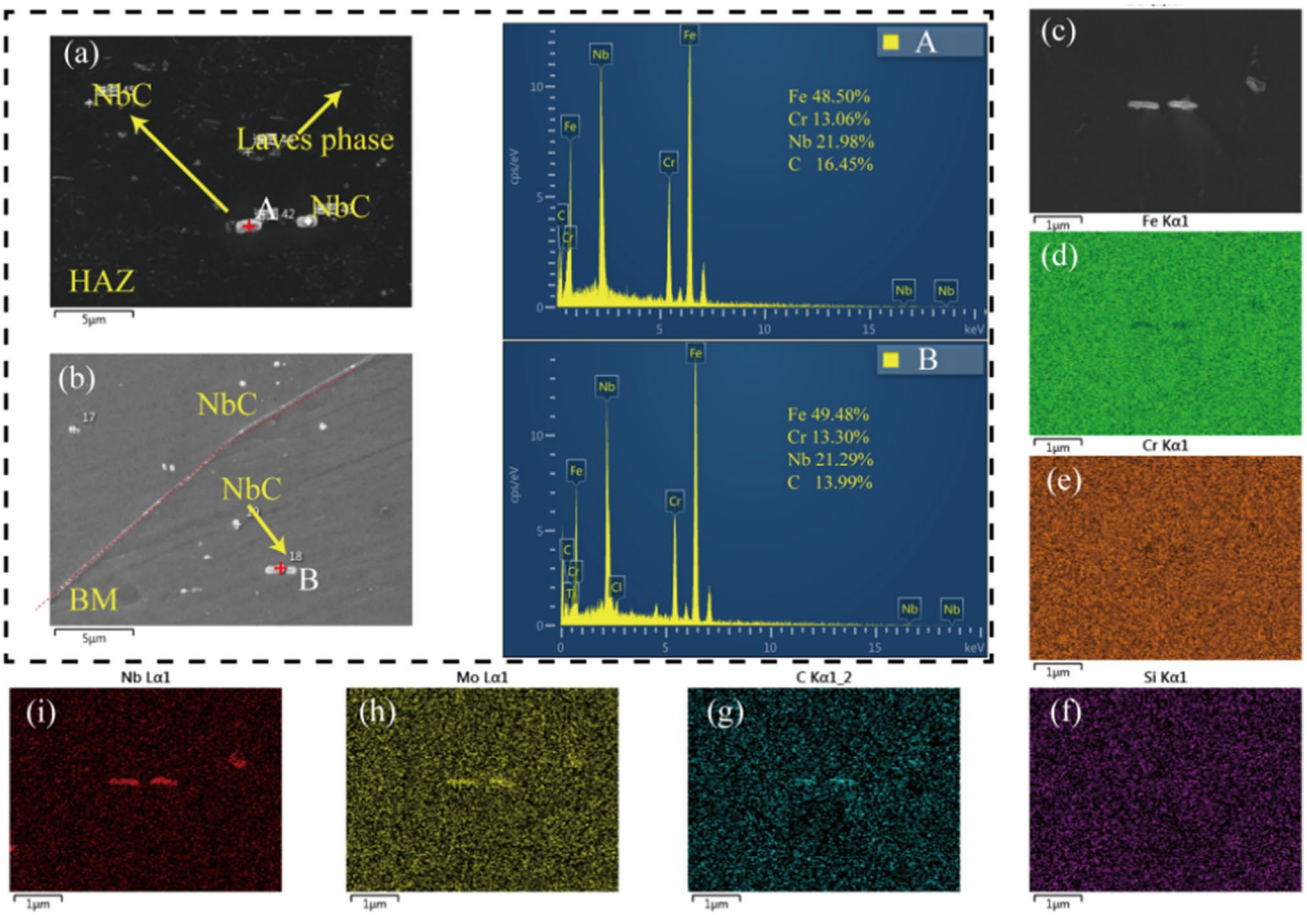

Fig.12 EDS analysis of precipitated phase in the HAZ of high-frequency pulse K-TIG joint: **a** EDS analysis of precipitated phase in HAZ; **b~h** elemental maps of selected area

Table 3 XRD results of precipitated phase

Precipitates	Peak locations (2θ)/Weld joints in different positions	
	WZ	HAZ
Laves (Fe_2Nb)	40.682° (103)	40.597° (103)
	43.450° (200)	43.307° (200)
x	39.856° (002)	39.856° (002)
	42.423° (330)	42.423° (330)
	64.327° (620)	64.327° (620)
σ	74.25° (333)	74.41° (333)
$a-Fe$	44.451° (110)	44.614° (110)
	65.022° (200)	64.931° (200)
	82.334° (211)	82.209° (211)
Laves(Fe_2Mo)	90.038° (206)	90.038° (206)
NbC	--	34.731° (111)

deformation, and fracture. This sequence indicates that both the BM and Joint No. 6 conform to the uniform yield type. The tensile strength of the BM measures 795 MPa, with an

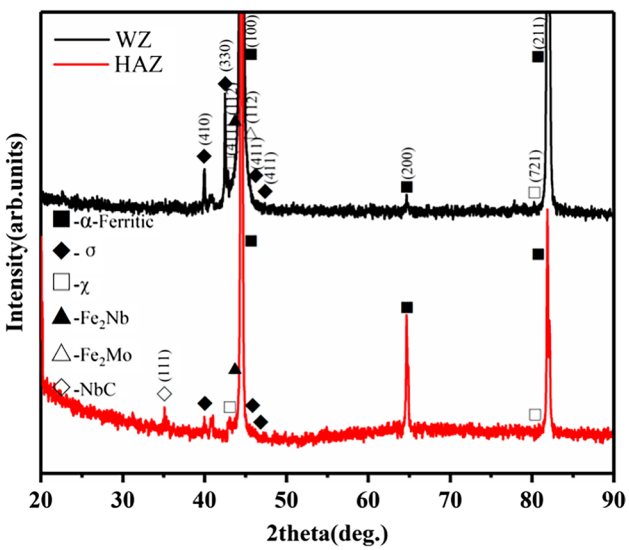

Fig. 13 XRD patterns of high-frequency pulse K-TIG WZ and HAZ

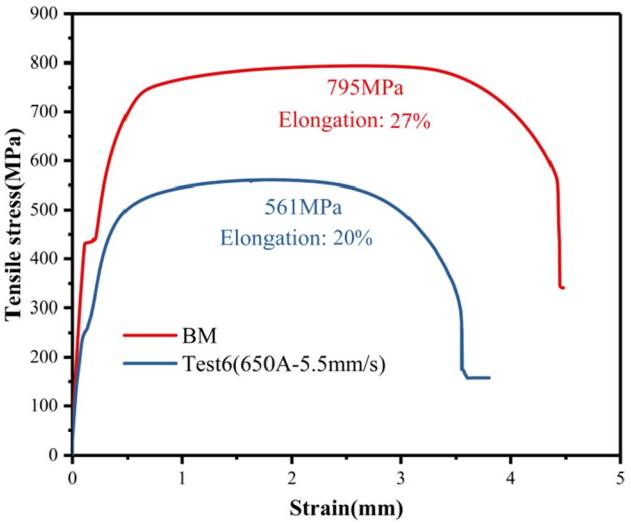

Fig. 14 Tensile curves of test 6 welded joints and BM

elongation of 27%. Conversely, Joint No. 6 exhibits a tensile strength of 561 MPa, which represents 71% of the BM, and an elongation of 20%. It is worth noting that although the tensile strength of the welded joint is lower than BM, its welding efficiency is significantly higher than that of the conventional fusion welding process [29].

Figures 15 and 16 illustrate the tensile fracture morphology of both the BM and Test 6 joints. The macroscopic fracture morphology of BM is presented in Fig. 15a and b, revealing the presence of a shear lip region and a fiber region. SEM was utilized to examine the fiber region of the BM, primarily constituted by extensive, deep equiaxial dimples and sporadic micropores (Fig. 15c, d). These observations suggest that the BM possesses commendable ductility. Figure 16a exposes the macro fracture topography of Test 6, characterized by cleavage planes and stratification, with the local microscopic fracture exhibiting a river pattern (Fig. 16b, c). Further magnification reveals a group of dimples in the microscopic fracture topography, with a large dimple formed by precipitated phase and smaller particles. During growth, smaller dimples merge with the free surface of the larger dimple (Fig. 16d). Comparatively, the

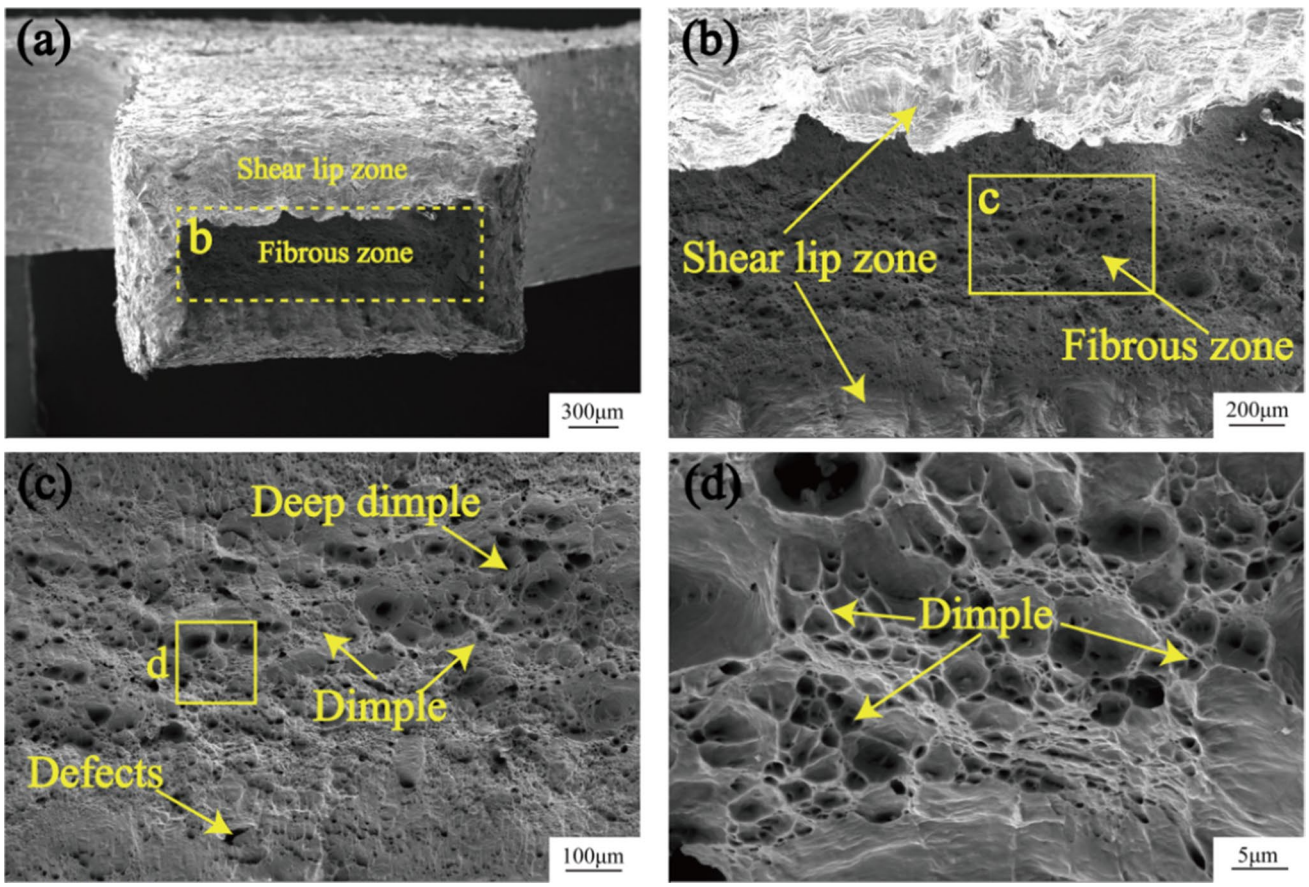

Fig. 15 Tensile fracture morphology of BM. **a** Macroscopic fracture morphology of BM; **b** shear lip region and fiber region of BM fracture; **c** partial enlarged view of **b**; **d** partial enlarged view of **c**

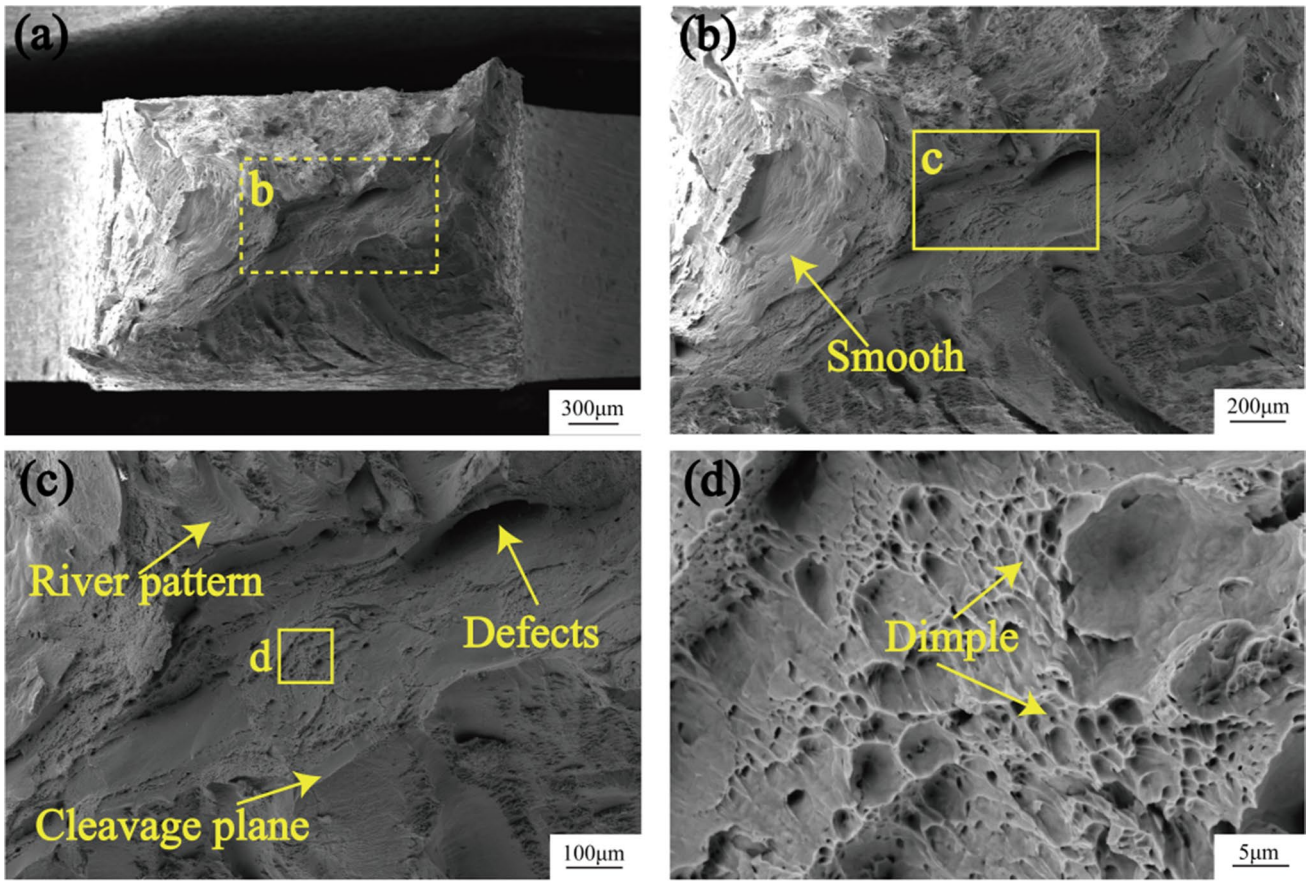

Fig. 16 No. 6 tensile fracture morphology of welded joints. **a** Macroscopic fracture morphology of weld joints; **b** partial enlarged view of **a**; **c** partial enlarged view of **b**; **d** partial enlarged view of **c**

dimples in fractured welds are smaller and more densely packed, which could potentially contribute to a decrease in elongation. The reduction in tensile properties is primarily associated with phase precipitation and grain coarsening. According to Hu et al. [37], the precipitation of brittle-hard phases could result in decreased impact toughness, tensile strength, and plasticity at room temperature.

3.3.2 Impact toughness

Impact toughness is indicative of a metal material's resistance to external impact forces. Due to the high-frequency pulse K-TIG welding process's HAZ being exceptionally narrow, sampling for impact toughness tests in this area is unfeasible. Consequently, tests are only conducted on the BM and samples with the notch located in the WZ. As indicated in Table 4, the BM's average impact toughness at room temperature is 69 J. In contrast, the average impact toughness for the No. 6 joint is 29 J, representing a 58% decrease compared to the BM.

Figure 17a illustrates the macroscopic impact fracture surface of the BM, characterized by a dark gray, fibrous appearance. At the microscopic level, the fracture surface displayed a profusion of dimples, as seen in Fig. 17b and c, indicative of ductile fracture. Figure 17d depicts the macroscopic impact fracture surface of joint number six, which is noticeably brighter, with distinct cleavage planes and tear ridges. Additionally, river patterns and cleavage steps are observed in these planes (Fig. 17e). The microscopic examination of this joint's fracture surface revealed numerous micropores and clusters of dimples (Fig. 17f), although these were smaller than those in the BM, suggesting a reduced

Table 4 Impact toughness test results

Test number	Size/mm	Test temperature/℃	Impact energy/J	Average/J	Notch location
BM	55×10×2.5	Room temperature	68, 70	69	Weld
No. 6	55×10×2.5	Room temperature	27, 32	29	Weld

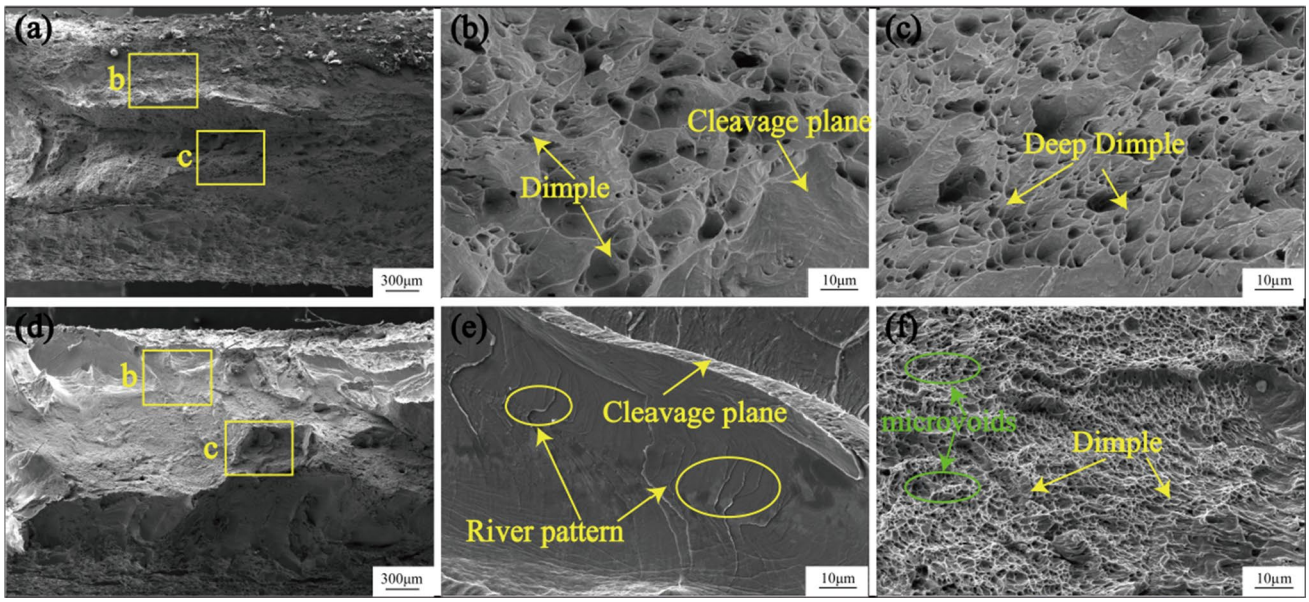

Fig. 17 Impact fracture morphology. **a~c** BM; **d~f** No. 6 welded joints

energy absorption capacity in joint number six during fracture. The coarsening of weld grains and precipitation of brittle, hard secondary phases diminish the impact toughness, particularly with significant σ phase precipitation at the grain boundaries. In comparison, high-frequency pulse K-TIG welding yields a finer microstructure with a reduced σ phase presence at the grain boundaries than constant-current K-TIG welding, thereby enhancing impact toughness as referenced in studies [23, 37].

4 Conclusions

The main conclusions are as follows:

(1) The high-frequency pulse K-TIG successfully completed the one-side welding with back formation of AISI 444 FSS with a thickness of 6 mm and obtained a good welding process window range. Research indicates that the heat input during the welding process is a pivotal factor in determining weld penetration. Furthermore, the welding current exerts a more substantial influence on weld penetration than welding speed, while the latter predominantly affects the width of the weld profile.

(2) The WZ and HAZ are primarily composed of ferrite and an assortment of secondary phases. These precipitated phases, identified as σ phases, x phases, and Laves phases, were discerned at the grain boundaries and within the grains of the WZ. The above precipitated phase was also observed in HAZ; besides, the elliptic precipitated phase was also observed, which was judged to be NbC. The origin of NbC appears to be the BM, a conclusion supported by XRD results. It is noteworthy that the high thermal conductivity of FSS and the pinning effect of NbC mitigate the likelihood of grain growth in the HAZ.

(3) The tensile strength of the high-frequency pulse K-TIG joint is measured at 561 MPa, representing 71% of the BM, with an elongation of 20%. Its impact toughness registers at 29 J, equivalent to 42% of the BM. The results show that the strength and toughness of the high-frequency pulse K-TIG FFS joint are lower than that of the BM, but still higher than that of other constant current K-TIG joints.

(4) With the development of industry, in order to meet the needs of enterprises for the production of low cost, high efficiency and high quality, the future FSS welding will develop to the high-efficiency welding of thick plates. High-frequency pulse K-TIG welding provides a new welding method to solve the high efficiency (deep penetration, autogenous welding) welding of FSS of medium and thick plate. Although the strength and ductile toughness of joints created by high-frequency pulse K-TIG welding surpass those of constant current K-TIG joints, the formation of columnar crystals within the weld can compromise the joint's ductile toughness to some degree. Consequently, refining the grain structure of high-frequency pulse K-TIG welds in FSS will be critical in addressing the performance issues of autogenous joints in medium and heavy plates. Currently, methods that introduce external energy fields during

the welding process have proven effective in enhancing weld properties. For instance, the application of a magnetic field, an efficient and simplified approach, generates thermal and force effects within the weld, provoking forced liquid metal flow within the molten pool and magnetic oscillation.

Author contribution All co-authors participated in the writing or guidance of the paper and played an important role.

Funding The present research work was financially supported by the Shenyang Collaborative Innovation Center Project for Multiple Energy Fields Composite Processing of Special Materials (Grant No. JG210027) and Shenyang Key Technology Special Project of "The Open Competition Mechanism to Select the Best Solution" (Grant No. 2022210101000827, 2022-0-43-048).

Data availability The datasets used or analyzed during the current study are available from the corresponding author on reasonable request.

Declarations

Consent to participate All co-authors are aware of the writing and publication of this article and agree to publish it.

Consent for publication All co-authors agree to publish this article.

Competing interests The authors declare no competing interests.

References

1. Vidyarthy RS, Dwivedi DK (2018) A comparative study on creep behavior of AISI 409 ferritic stainless steel in as-received and as-welded condition (A-TIG and M-TIG). Mater Today 5(9):17097–17106. https://doi.org/10.1016/j.matpr.2018.04.117
2. Ma L, Hu SS, Hu B, Shen JQ, Wang Y (2014) Activating flux design for laser welding of ferritic stainless steel. Trans Tianjin Univ 20:429–434. https://doi.org/10.1007/s12209-014-2243-5
3. Mousazadeh MA, Derakhshandeh-Haghighi R (2020) Autogenous tungsten inert gas welding of 430 ferritic stainless steel: the effect of inter-pass temperature on microstructure evolution and mechanical properties. J Mater Eng Perform 29:7807–7820. https://doi.org/10.1007/s11665-020-05281-z
4. Ranjbarnodeh E, Hanke S, Weiss S, Fischer A (2012) Effect of welding parameters on the heat-affected zone of AISI409 ferritic stainless steel. Int J Min Met Mater 19:923–929. https://doi.org/10.1007/s12613-012-0648-5
5. Lakshminarayanan AK, Balasubramanian V (2012) Evaluation of microstructure and mechanical properties of laser beam welded AISI 409M grade ferritic stainless steel. J Iron Steel Res Int 19(1):72–78. https://doi.org/10.1016/S1006-706X(12)60050-8
6. Ahmed MMZ, El-Sayed Seleman MM, Shazly M et al (2019) Microstructural development and mechanical properties of friction stir welded ferritic stainless steel AISI 409. J Mater Eng Perform 28:6391–6406. https://doi.org/10.1007/s11665-019-04365-9
7. Silva CC, Farias JP, Miranda HC et al (2008) Microstructural characterization of the HAZ in AISI 444 ferritic stainless steel welds. Mater Charact 59(5):528–533. https://doi.org/10.1016/j.matchar.2007.03.011
8. Akita M, Uematsu Y, Kakiuchi T et al (2018) Joint microstructures mechanical properties and fatigue behaviour of ferritic stainless steel sus 430 welds with different filler metals. Weld Int 32(6):427–435. https://doi.org/10.1080/09507116.2017.1346860
9. Zhang H, Hu S, Shen J et al (2015) Microstructures and mechanical properties of 30Cr-4Mo ferritic stainless steel joints produced by double-pulsed gas metal arc welding. Int J Adv Manuf Tech 80:1975–1983. https://doi.org/10.1007/s00170-015-7173-4
10. Venkatesan MV, Murugan N, Sam S et al (2013) Effect of heat input on macro micro and tensile properties of flux cored arc welded ferritic stainless steel joints. Trans Indian Inst Met 67(3):375–383. https://doi.org/10.1007/s12666-013-0358-3
11. Vidyarthy RS, Dwivedi DK, Vasudevan M (2017) Influence of M-TIG and A-TIG welding process on microstructure and mechanical behavior of 409 ferritic stainless steel. J Mater Eng Perform 26:1391–1403. https://doi.org/10.1007/s11665-017-2538-5
12. Vidyarthy RS, Kulkarni A, Dwivedi DK (2017) Study of microstructure and mechanical property relationships of A-TIG welded P91–316L dissimilar steel joint. Mater Sci Eng A 695:249–57. https://doi.org/10.1016/j.msea.2017.04.038
13. Anh NV, Tashiro S, Hanh BV, Tanaka M (2018) Experimental investigation on the weld pool formation process in plasma keyhole arc welding. J Phys D: App Phys 51(1). https://doi.org/10.1088/1361-6463/aa9902
14. Prasad KS, Chalamalasetti SR, Damera NR (2015) Application of grey relational analysis for optimizing weld bead geometry parameters of pulsed current micro plasma arc welded inconel 625 sheets. Int J Adv Manuf Technol 78:625–632. https://doi.org/10.1007/s00170-014-6665-y
15. Lakshminarayanan AK, Shanmugam V, Balasubramanian V (2009) Effect of autogenous arc welding processes on tensile and impact properties of ferritic stainless steel joints. J Iron Steel Res Int 16(1):62–68. https://doi.org/10.1016/S1006-706X(09)60012-1
16. Zhu SC, Wang BS, Bi HY, Yan B (2018) Performance evaluation of 00Cr11NbTi perforated-plasma-arc-welded joint. Baosteel Tech Res 12(02):13–16
17. KÖSE, C, Topal C (2019) Effect of post weld heat treatment and heat input on the microstructure and mechanical properties of plasma arc welded AISI 410S ferritic stainless steel. Mater Res Express 6(6). https://doi.org/10.1088/2053-1591/ab09b6
18. Dong ZH, Li YW, Lee BY et al (2022) Research status of welding technology of ferritic stainless steel. Int J Adv Manuf Technol 118:2805–2831. https://doi.org/10.1007/s00170-021-08128-6
19. Hariharan SJ, Vigneshwar M, Selvamani ST, Shanmugam K, Palanikumar K (2019) Optimizing the plasma arc welding process parameters to attain the minimum corrosion rate in the AISI 409M grade ferritic stainless steel autogenous joints. Mater Today: Proc 16:1259–1270. https://doi.org/10.1016/j.matpr.2019.05.223
20. Lakshminarayanan AK, Balasubramanian V, Reddy GM (2011) Microstructure and mechanical properties of electron beam-welded AISI 409M-grade ferritic stainless steel. Int J Adv Manuf Technol 55(1–4):153–162. https://doi.org/10.1007/s00170-010-3044-1
21. Lakshminarayanan AK, Balasubramanian V (2012) Influences of welding processes on microstructure and mechanical properties of modified 12 wt % Cr ferritic stainless steel. Inter J Manuf Rsrch 7(4):7679–7687. https://doi.org/10.1504/IJMR.2012.050100
22. Liu LL, Hu SS, Shen JQ (2015) Effect of laser welding heat input on microstructure and properties of 26Cr-3.5Mo ferritic stainless steel. Chin J Lasers 42(02):101-107. JournalArticle/5b3b8033c095d70f00791477
23. Xie Y, Cai YC, Zhang X et al (2018) Characterization of keyhole gas tungsten arc welded AISI 430 steel and joint performance optimization. Int J Adv Manuf Technol 99:347–361. https://

doi.org/10.1007/s00170-018-2257-6 https://doi.org/10.1007/s00170-018-2257-6
24. Fei Z, Pan Z, Cuiuri D et al (2019) Microstructural characterization and mechanical properties of K-TIG welded SAF2205/AISI316L dissimilar joint. J Manuf Process 45:340–355. https://doi.org/10.1016/j.jmapro.2019.07.017
25. Han L, Han T, Chen G et al (2021) Influence of heat input on microstructure, hardness and pitting corrosion of weld metal in duplex stainless steel welded by keyhole-TIG. Materials Characterization 175:111052. https://doi.org/10.1016/j.matchar.2021.111052
26. Feng YQ, Luo Z, Liu ZM et al (2015) Keyhole gas tungsten arc welding of AISI 316L stainless steel. Mater Des 85:24–31. https://doi.org/10.1016/j.matdes.2015.07.011
27. Lathabai S, Jarvis BL, Barton KJ (2008) Keyhole gas tungsten arc welding of commercially pure zirconium. Sci Technol Weld Join 13:573–581. https://doi.org/10.1179/136217108X329296
28. Lathabai S, Jarvis BL, Barton KJ (2001) Comparison of keyhole and conventional gas tungsten arc welds in commercially pure titanium. Mater Sci Eng A 299:81–93. https://doi.org/10.1016/S0921-5093(00)01408-8
29. Fei ZY, Pan ZX, Cuiuri D et al (2018) Investigation into the viability of K-TIG for joining armour grade quenched and tempered steel. J Manuf Process 32:482–493. https://doi.org/10.1016/j.jmapro.2018.03.014
30. Cui S, PangS Pang D et al (2021) Influence of welding speeds on the morphology, mechanical properties, and microstructure of 2205 DSS welded joint by K-TIG welding. Materials 14(12):3426. https://doi.org/10.3390/ma14123426
31. Zmitrowicz P, Kawiak M, Kochmański P et al (2021) Microstructure and mechanical properties of welded joints of 1.4462 duplex steel made by the K-TIG method. Materials 14(24):7868. https://doi.org/10.3390/ma14247868
32. Cui S, Liu Z, Fang Y et al (2017) Keyhole process in K-TIG welding on 4 mm thick 304 stainless steel. J Mater Process Technol 243:217–228. https://doi.org/10.1016/j.jmatprotec.2016.12.027
33. Unnikrishnan R, Idury KS, Ismail TP et al (2014) Effect of heat input on the microstructure, residual stresses and corrosion resistance of 304L austenitic stainless steel weldments. Mater Charact 93:10–23. https://doi.org/10.1016/j.matchar.2014.03.013
34. Venkatesan MV, Murugan N, Sam S et al (2014) Effect of heat input on macro, micro and tensile properties of flux cored arc welded ferritic stainless steel joints. T Indian I Metals 67:375–383. https://doi.org/10.1007/s12666-013-0358-3
35. Chen SY, Liu ZM, Zhao XC et al (2019) Cathode-focused high-current arc: heat source development with stable keyhole in stationary welding. Int J Heat Mass Trans 143:118475. https://doi.org/10.1016/j.ijheatmasstransfer.2019.118475
36 Sourmail T (2001) Precipitation in creep austenitic stainless steels. Mater Sci Technol 17:1–13. https://doi.org/10.1179/026708301101508972
37. Lu HH, Luo Y, Guo HK et al (2018) Microstructural evolution and mechanical properties of 27Cr-4Mo-2Ni ferritic stainless steel during isothermal aging. Mater Sci Eng A 735:31–39. https://doi.org/10.1016/j.msea.2018.08.031
38. Ge J, Liu X, Liu L (2022) Influence of brittleness and forming characteristics on properties of ultra-pure ferritic stainless steel. Chin Metall 04:9–20. https://doi.org/10.13228/j.boyuan.issn1006-9356.20210684
39. Qu HP, Lang YP, Chen HT et al (2012) The effect of precipitation on microstructure, mechanic properties and corrosion resistance of two UNS S44660 ferritic stainless steels. Mat Sci Eng A-Struct 534:436–445. https://doi.org/10.1016/j.msea.2011.11.091
40. Ma L (2015) Study on microstructure, properties and processing behavior of super ferritic stainless steel. PhD Dissertation, Tianjin University
41. Ma L, Hu SS, Shen JQ (2016) Characterisation of precipitates formed in 26% Cr super ferritic stainless steel. Ironmak Steelmak 43(10):752–757. https://doi.org/10.1080/03019233.2016.1165486
42. Juuti T, Rovatti L, Mäkelä A et al (2014) Influence of long heat treatments on the laves phase nucleation in a type 444 ferritic stainless steel. J Alloy Comp 616:250–256. https://doi.org/10.1016/j.jallcom.2014.06.201
43. Yan HT, Bi HY, Li X (2009) Effect of microstructure and properties of ferritic stainless steel. Iron Steel 44(1):59–62+94
44. Saha R, Ray RK, Bhattacharjee D (2007) Attaining deep drawability and non-earing properties in Ti+Nb interstitial-free steels through double cold rolling and annealing. Scripta Mater 57(3):257–260. https://doi.org/10.1016/j.scriptamat.2007.03.055